Molecular Sieves

DOI: 10.1002/anie.201006031

Architecture-Dependent Distribution of Mesopores in Steamed Zeolite Crystals as Visualized by FIB-SEM Tomography**

*Lukasz Karwacki, D. A. Matthijs de Winter, Luis R. Aramburo, Misjaël N. Lebbink, Jan A. Post, Martyn R. Drury, and Bert M. Weckhuysen**

Zeolites are one of the major pillars of the petrochemical industry. Their precisely defined porous system, resistance towards harsh reaction conditions, and excellent acidic properties make them indispensible in many catalytic processes.[1–6] A handful of industrially relevant zeolites, including zeolite Y and ZSM-5, are extensively used in processes such as hydrocarbon cracking, isomerization, and alkylation.[7–9] Therefore, as the unique catalytic properties of zeolites rely to a great extent on molecular diffusion and accessibility of acid sites, a great number of studies has focused on the improvement of these properties.[10,11] Examples include the synthesis of nanocrystals and exfoliating layered zeolites.[12–14] Although the above-mentioned methods allow the fine tuning of the material accessibility, the synthesis complexity and related costs most probably exceeds the costs of industrially applicable materials.

In contrast, cheap and efficient dealumination by steaming and alkali-based desilication has become an efficient approach in boosting the molecular uptake of zeolites.[15–18] While both methods are fairly simple in terms of enhancing the molecular diffusion, until now not much is known about the uniformity and the size variations of the obtained mesopores. The main direct approach makes use of electron tomography (ET) and is still limited to materials not exceeding a few hundred nanometers,[19–21] while N_2 physisorption measurements only provide average information on the mesopore volume.[22] Furthermore, as known from our previous study on the molecular diffusion barriers in ZSM-5 zeolites, the crystal's morphology and internal architecture define areas where straight and sinusoidal channels are open to the surface. Consequently, individual zeolite crystals differ in their overall material accessibility and related catalytic behavior.[23–25]

Here, we describe for the first time the powerful combination of focused ion beam (FIB) and scanning electron microscopy (SEM) tomography to characterize porous solids, such as zeolites. As will be shown below, the approach leads to new quantitative insight into the type of mesopores (length, width, and morphology) generated in steamed zeolites. For this purpose, we have focused our attention on individual coffin-shaped ZSM-5 crystals with dimensions of $100 \times 20 \times 20\ \mu m^3$, in which mesoporosity has been introduced by steaming.

In a first set of experiments the FIB milled cross-sections of three distinct regions of the ZSM-5 parent crystal (denoted as crystal ZSM-5-P) were prepared. The blue and red areas shown in Figure 1a correspond to the parts of the crystal with straight and sinusoidal channels open to the surface, respectively, whereas the green rectangle refers to the region where straight channels are covered by the 90° rotational barrier. As expected, non-steamed ZSM-5-P does not show any damage of the different regions of the crystal or the presence of mesopores, proving that zeolite pretreatment does not influence the characteristics of the material (Figure 1b). On the contrary, a study of the near surface regions of the steamed crystal (ZSM-5-S) depicted in Figure 1c shows a significant influence of the steaming post-treatment resulting in the presence of vast areas of mesoporosity (yellow contours).

Examination of the collected images provides clear evidence of the non-uniform mesopore distribution present in the three areas of the steamed ZSM-5 sample. More specifically, region A originating from the tip of the ZSM-5 crystal contains a smaller number of mesopores than regions B and C. As the cross-sections collected from the near-surface regions prove the successfulness of the steam treatment, it is relevant to study mesopore distribution in the center of the dealuminated crystal in detail. For this purpose, a second steamed ZSM-5 crystal was investigated. The results are summarized in Figure 2.

As illustrated in Figure 2c and d, dealumination of the ZSM-5 crystals led to the generation of mesoporosity in the entire crystal volume. More specifically, regions III and IV originating from the cross-sections dissected from the middle depths of the crystal center and tip provide clear proof of the occurrence of mesopores. Thus, the steaming treatment

[*] Dr. L. Karwacki,[+] L. R. Aramburo, Prof. Dr. B. M. Weckhuysen
Inorganic Chemistry and Catalysis Group
Debye Institute for Nanomaterials Science
Faculty of Science, Utrecht University
Sorbonnelaan 16, 3584 CA Utrecht (The Netherlands)
Fax: (+31) 30-251-1027
E-mail: b.m.weckhuysen@uu.nl

D. A. M. de Winter,[+] Dr. M. N. Lebbink, Dr. J. A. Post
Biomolecular Imaging, Institute of Biomembranes
Faculty of Sciences, Utrecht University
3584 CH Utrecht (The Netherlands)

Prof. Dr. M. R. Drury
Department of Earth Sciences, Faculty of Geosciences
Utrecht University, 3508 TA Utrecht (The Netherlands)

[+] These authors contributed equally to this work.

[**] We thank NWO for financial support (CW-NWO Top grant) and a large investment subsidy for the Dualbeam microscope. Machteld Mertens (ExxonMobil, Machelen, Belgium) is acknowledged for providing the ZSM-5 crystals. FIB-SEM = focused ion beam scanning electron microscopy.

Supporting information for this article is available on the WWW under http://dx.doi.org/10.1002/anie.201006031.

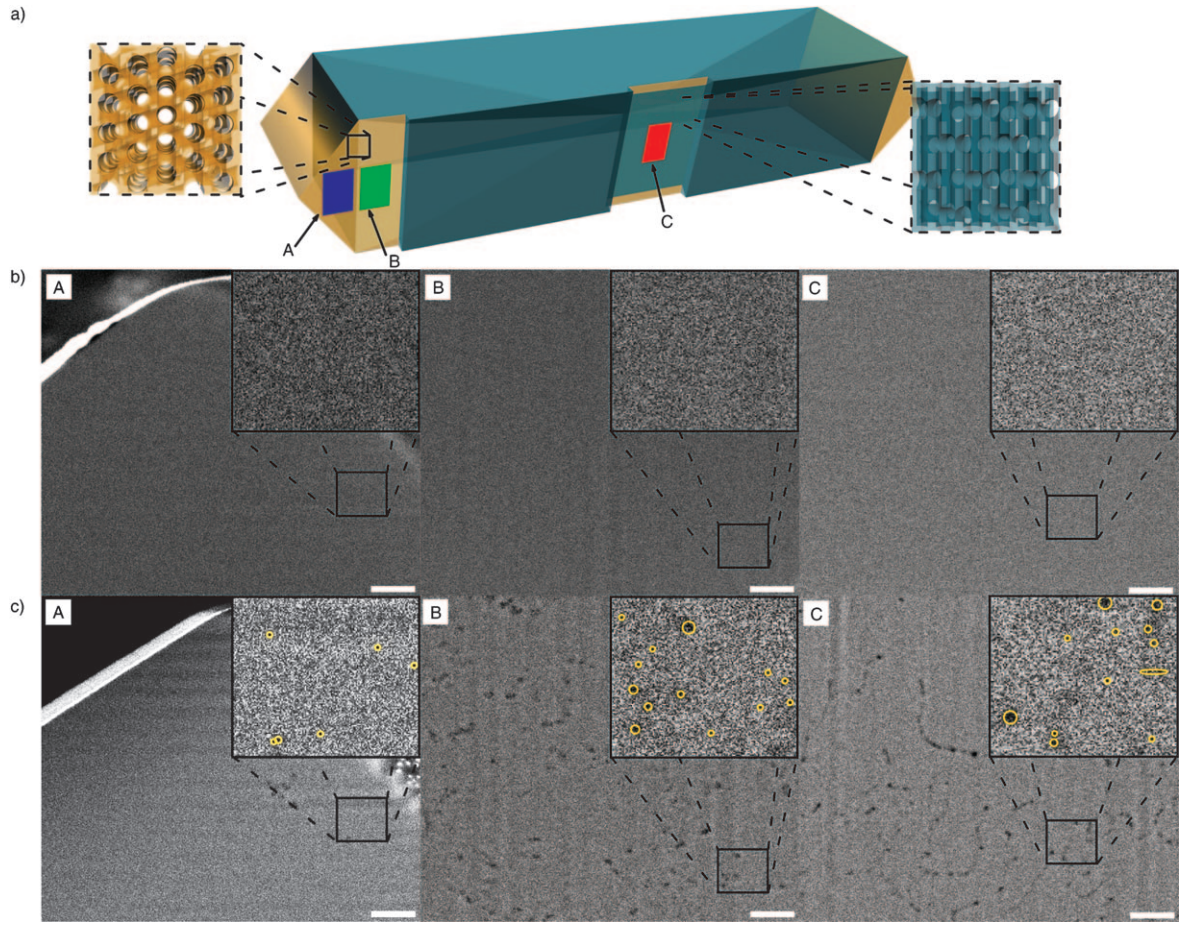

Figure 1. a) Schematic of a ZSM-5 individual crystal from which the FIB cross-sections were milled. Studied areas A–C are highlighted as blue, green, and red rectangles, respectively. Straight and sinusoidal pores open to the surface are indicated by the orange and light blue areas, respectively. b) SEM images of the three studied cross-sections (A–C) belonging to the parent crystal, together with the 16× digitally zoomed-in insertions. Scale bar is 300 nm. c) Same as (b), but for steamed crystal. Recorded mesopores are highlighted in the SEM insertions with the yellow contours.

employed ensures a successful steaming of the entire µm-sized ZSM-5 crystals (see Figure S1 in the Supporting Information for magnifications of regions I–IV) enabling us to investigate in detail the influence of the internal architecture of the zeolite crystals on the generation and three-dimensional distribution of mesopores.

In this respect, it is important to note that the cross-sections collected from the near surface regions (I and II) exhibit differences in the mesoporosity distribution as compared to the middle depth of the crystal (III and IV). In particular, the SEM image of area I in Figure 2c demonstrates the presence of mesopores parallel to the milled crystal surface. This behavior has been found to be common for the near-surface areas of the crystal's center and is observed in both studied samples (region C in Figure 1c and area I in Figure 2c). A possible explanation of the above-mentioned presence of two-dimensional mesoporosity is the damage of the straight channels open to the zeolite exterior. From previous studies[25,26] it is known that the surface of large ZSM-5 crystals is not atomically flat, but rather consists of unit cells formed in steps, kinks, and terraces, leading to the variations of surface height. Therefore, upon steaming the straight channels parallel to the crystal surface and open to the crystal exterior will be susceptible towards aluminum extraction and translate into mesopores parallel to the crystal surface in the first few hundred nm of the crystal volume.

To obtain statistical information about the pore size distribution, both steamed ZSM-5 crystals were imaged with SEM. A statistical analysis of the two different crystals is presented in Figure 3a and Table S1, which allow us to compare the average pore size distribution within the studied regions A–C.

As shown in Figure 3a, analysis of the materials revealed a significant dependency between the crystal region and the amount and diameter of the generated mesopores. The dominating mesopores sizes in region A vary between 5.2 nm and 7.8 nm with an average size of all mesopores of about 6.2 nm. However, a few mesopores up to 20 nm can be found. Similar analysis of regions B and C reveals that the average diameter of all mesopores increases to 8.2 and 8 nm, while the maximal diameters of the mesopores were found to be 50 nm and 35 nm, respectively. Statistical analysis of the two steamed crystals revealed that region A contains about 23% of the overall number of mesopore channels found in all three studied regions, whereas regions B and C have 40% and 37% of all mesopores, respectively. Strikingly, as can be seen

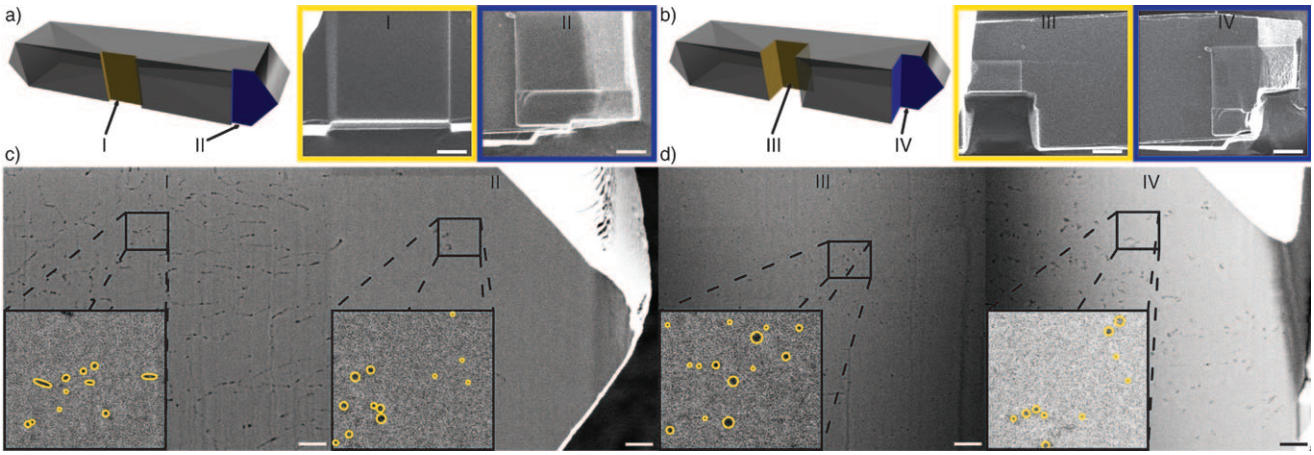

Figure 2. a) Schematic of a dealuminated ZSM-5 crystal with FIB cross-section areas chosen for the SEM imaging near the surface of the material and SEM images of areas I and II showing the different stages of the FIB cross-sections milling. Scale bar = 5 μm. b) Same as (a), but for the cross-sections dissected from the center of the crystal and areas III and IV. c, d) SEM images of the studied cross-sections of the ZSM-5 crystal tip and the crystal body. Areas indicated as I–IV refer to the location and depth of the cross-sections as shown in (a) and (b). Insertions are 64× zoomed-in areas indicated by the black rectangles. Scale bar = 400 nm. Recorded mesopores are highlighted in the SEM insertions with the yellow contours.

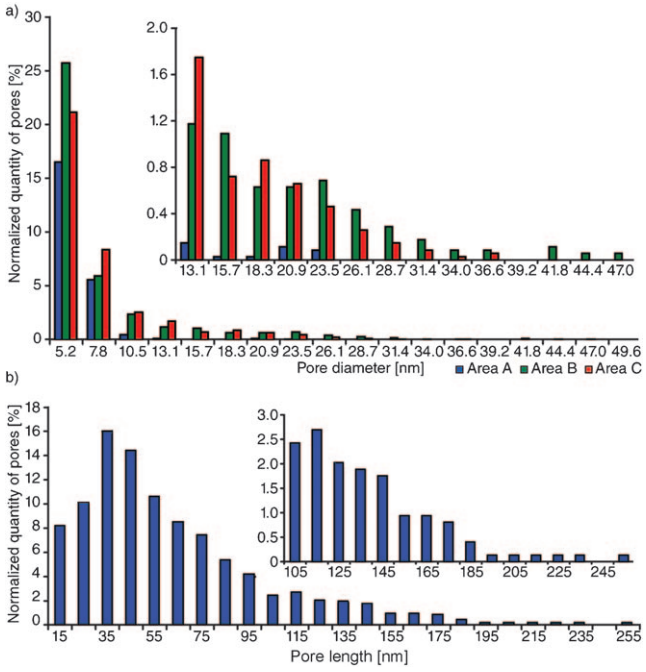

Figure 3. a) Normalized diameter of the pores for regions A–C in Figure 1 showing the dominating population of pores in the 5–50 nm region. Insertion: zoom-in into the pores above 13 nm. b) An average length of the mesopores based on approximately 750 reconstructed mesopores from the volume of steamed ZSM-5 crystal discussed further (Figure S4). Insertion: zoom-in into the pores longer than 100 nm. The error range for each pore length data point equals ±5 nm (i.e. a slice thickness equal to 10 nm). See Supporting Information for details on the measurements accuracy.

in Table S1 and Figure S2, the distribution of mesopores sizes in all regions reveals that more than 84% of all recorded mesopores do not exceed 10 nm in diameter.

To better understand the non-uniform dealumination of the ZSM-5 crystals, local Al distribution has to be discussed. As the synthesis of the large and well-defined zeolite crystals is difficult to control on the chemical composition level, numerous studies have reported the presence of the Al zoning within the zeolite material.[27–29] A gradient in the Al (or Si) content within the material volume would have a significant impact on the zeolite's local susceptibility towards the steam treatment and obscure the understanding of the micropore orientation influence on the dealumination of ZSM-5. Therefore it is important to underline that the parent ZSM-5 crystals discussed here contain an equal amount of Al throughout the crystal,[30] allowing the mesoporosity to be related to the crystals intergrowth architecture.

According to the obtained pore size distribution, mesopore generation by steaming is highly influenced by the orientation of the micropores and thus the internal architecture of the crystal. More specifically, the interior of the straight channels (open to the surface in the orange regions of the crystal in Figure 1a; area A) seem to be much more resistant towards dealumination than the sinusoidal channels (light blue regions in Figure 1a) exposed to the crystal's exterior in region C.[25,31] Remarkably, region B, being the area with straight channels sheltered in the parent ZSM-5 by the 90° rotational barrier (Figure 1a) is not only the part of the crystal that presents the highest number of mesopores, but also contains the most heterogeneous mesopore size distribution as compared to the other crystal regions.

Apparently, extraction of the debris originating from zeolite dealumination is much more hindered within the straight pores than in the sinusoidal channel, leading to the varying pore size distribution. Interestingly, upon steaming, the 90° rotational barrier starts acting as the preferential path for diffusion and facilitates the debris removal through the straight pores beneath it. This behavior can be seen by comparing regions II and IV in Figure 2c and d. Here, the image of the cross-section collected from the near-surface region consists of a small amount of mesopores (region II), however, the image recorded from the middle of the same crystal proves clearly the presence of a high number of mesopores (regions B in Figure 1a and IV in Figure 2d).

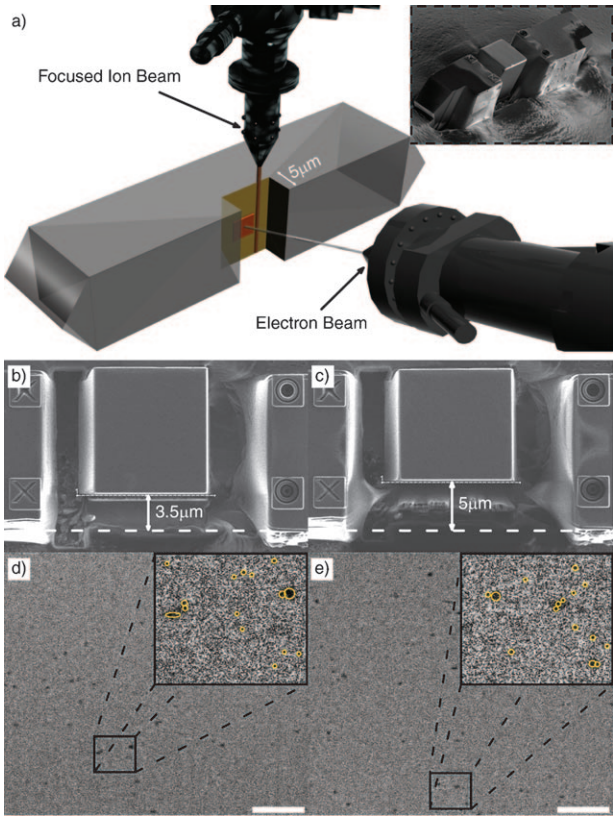

Figure 4. a) Individual steamed ZSM-5 crystal during FIB-SEM tomography. Focused ion beam (top) subsequently removes (10 ± 2) nm thick cross-sections from the plane normal to the crystal's surface, while the electron-beam images of 5 × 5 µm are indicated with the red square. Insertion shows a steamed crystal after FIB cross-section milling. b, c) SEM images illustrating the beginning and the end of the volume studied by FIB-SEM tomography. The difference between the thickness of the material in images (b) and (c) is 1.5 µm. d, e) SEM images of the first and the last cross-section collected from the analyzed volume of the steamed ZSM-5.

In view of obtaining 3-D information on the length and morphology of the mesopores generated in the steamed ZSM-5 crystals, FIB-SEM tomography was applied as a novel method for characterization of porous materials. Figure 4 presents the combination of the subsequent FIB milling and SEM imaging of the crystal. This approach allowed subsequent milling and imaging of the steamed crystal's volume and visualization of mesopores in 3-D.

Subsequently, a stack of 150 consecutive cross-sections separated from each other (10 ± 2) nm with the surface area of about to 5 × 5 µm^2 was collected (red square in Figure 4a). Next, the digital SEM images were aligned, and the clearly visible mesopores were manually identified in all the layers, leading to the reconstruction of a studied zeolite volume. This is shown in Figure S3. Following this methodology a 5 × 5 × 1.5 µm^3 volume of an individual steamed ZSM-5 crystal was reconstructed in 3-D, illustrating the presence of approximately 750 mesopores of length exceeding 10 nm. The result is given in Figure S4.

However, before the reconstructed volumes will be analyzed, it is important to point out that mesopores with a diameter smaller than 10 nm could not be visualized in two consecutive micrographs. Therefore, approximately 84% of the overall population of mesopores (Table S1) cannot be resolved by the FIB-SEM tomography and are not included in the 750 pores discussed further on. Nevertheless, it is important to mention the impact of the sphere-like mesopores with a diameter below 10 nm. Owing to the nature of their morphology they are only connected through the micropores and therefore do not significantly enhance the molecular diffusion.

The lengths of the reconstructed mesopores vary in the range of 10 to 260 nm, while their width is between 10 and 50 nm. From the visualized population of mesopores (Figure S4) approximately 630 of them (85%) are in the range of 10 to 100 nm, while only 1% rises above 200 nm (Figure 3b). Considering that even the longest recorded mesopores are enclosed within 250 nm, therefore not longer than the 1.25% of the average width of the crystals, it is important to underline the uniformity of the steaming process and distribution of the mesopores across the whole crystal, as shown in Figure 2.

To better understand the porous distribution and assess the average morphology of the studied mesopores, Figure 5 shows a reconstructed representation of the 750 × 750 × 200 nm^3 subset of the aforementioned volume of the steamed ZSM-5. Here 11 resolved mesopores with a width ranging from 15 to 20 nm and a length below 60 nm are shown. As shown in Figure S3, overlaying of the subsequent FIB-SEM tomography images allows visualization of the external contour of the mesopores recorded in the ZSM-5 steamed crystals. However, to assess the 3-D morphology of the mesopores, digital meshing of the pores surface is required. This is illustrated in Figure 5b and c, in which the shape and form of two examples of mesopores are shown.

From the close investigation of the reconstructed mesopores, it becomes apparent that both the position and morphology are random. However, the long axis of the mesopores always aligns with the direction of the pores open to the crystal's surface (normal to the cross-section plane). Figure S5 illustrates the above-mentioned relation. Strikingly, out of the 750 mesopores found in the steamed ZSM-5 crystal's volume (between 10 and 250 nm), more than 87% (blue data points) do not deviate more than 50 nm from the direction of the sinusoidal micropores opened to the surface, while only 12% (green data points) and 1% (red data points) vary between 50–100 and 100–150 nm, respectively. This suggests that the majority of the large mesopores are 1-D and follow the sinusoidal micropores open to the zeolite surface. Therefore, upon dealumination, the shortest path for debris removal is chosen.

Summarizing, we have shown the presence, length/width distribution and morphology of mesopores in steamed ZSM-5 crystals by FIB-SEM tomography. Our novel approach allowed the visualization of the 3-D distribution of mesopores and it has been found that sinusoidal zeolite channels are much more susceptible towards dealumination than the straight zeolite channels, resulting in an internal architecture-dependent distribution of mesopores within steamed ZSM-5 crystals. It has been experimentally visualized that the 90° rotational barrier facilitates the dealumination debris

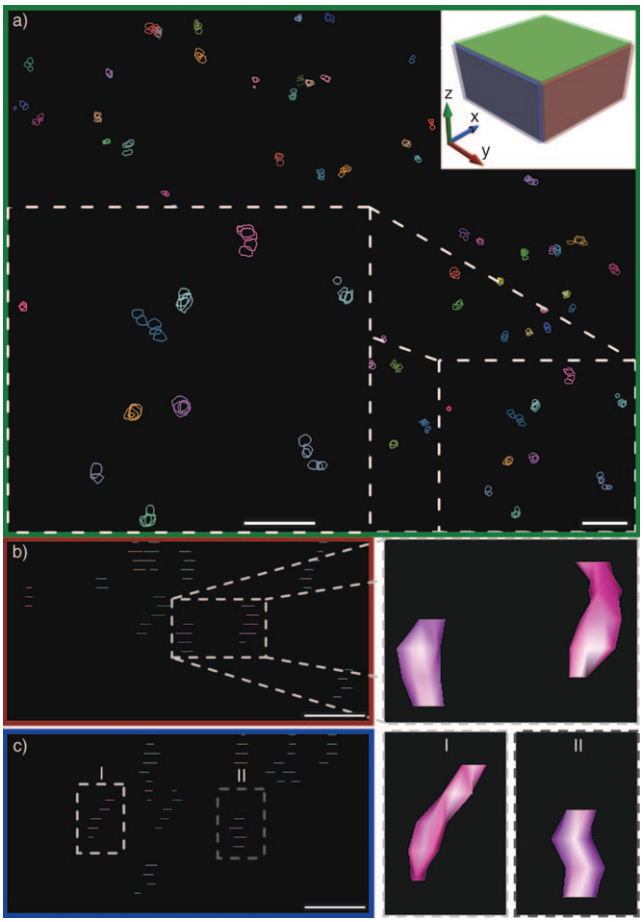

Figure 5. a) A reconstructed distribution of mesopores in the $750\times750\times200$ nm^3 sub-volume of steamed ZSM-5 crystal. Plane *xy* is shown; the upper right corner insertion indicates the orientation of the *xy*, *xz*, and *yz* planes as green, red, and blue rectangles, respectively. The ×2 zoomed-in area of the section shown in the right bottom corner of the *xy* plane shows a group of 11 reconstructed mesopores. Scale bars = 60 nm. Surface of indicated (traced) mesopores is not rendered allowing visualization of their overlay. b,c) Projection of the mesopores to the *xz* and *yz* planes, respectively. Each layer indicates the consecutive cross-sections plane recorded by SEM tomography. Zoomed-in area focuses on two pores with rendered surface. Scale bars are 50 nm. For more detailed information about the 3-D pores distribution we refer to Figure S2 and Movie S1.

removal, opens the straight micropores, and enhances the mesoporosity generation. The long axis of the mesopores always correlates with the axis of the micropores open to the crystal's surface, thus indicating that the shortest path for the removal of dealuminated material residues is preferred. In addition, the FIB-SEM tomography method does not call for lamella preparation and is generally applicable to porous materials with a thickness beyond hundreds of nanometers. The method resolution, however, is currently limited to approximately 5.2 nm, but it can be expected that in the near future the visualization of smaller mesopores will become within reach.

Received: September 26, 2010
Published online: January 7, 2011

Keywords: crystal intergrowth · scanning probe microscopy · mesoporosity · tomography · zeolites

[1] A. Corma, *Chem. Rev.* **1995**, *95*, 559.
[2] J. M. Thomas, *Sci. Am.* **1992**, *266*, 112.
[3] M. A. den Hollander, M. Wissink, M. Makkee, J. A. Moulijn, *Appl. Catal. A* **2002**, *223*, 85.
[4] J. M. Thomas, R. Raja, G. Sankar, R. G. Bell, *Nature* **1999**, *398*, 227.
[5] A. Corma, A. Martinez, *Adv. Mater.* **1995**, *7*, 137.
[6] J. E. Naber, K. P. de Jong, W. H. J. Stork, H. Kuipers, M. F. M. Post, *Stud. Surf. Sci. Catal.* **1994**, *84*, 2197.
[7] T. F. Narbeshuber, H. Vinek, J. A. Lercher, *J. Catal.* **1995**, *157*, 388.
[8] J. Abbot, A. Corma, B. W. Wojciechowski, *J. Catal.* **1985**, *92*, 398.
[9] Y. Ono, T. Baba, *Catal. Today* **1997**, *38*, 321.
[10] F. Schüth, *Angew. Chem.* **2003**, *115*, 3730; *Angew. Chem. Int. Ed.* **2003**, *42*, 3604.
[11] J. Pérez-Ramírez, C. H. Christensen, K. Egeblad, J. C. Groen, *Chem. Soc. Rev.* **2008**, *37*, 2530.
[12] L. Tosheva, V. P. Valtchev, *Chem. Mater.* **2005**, *17*, 2494.
[13] A. Corma, V. Fornes, S. B. Pergher, T. L. M. Maesen, J. G. Buglass, *Nature* **1998**, *396*, 353.
[14] A. Corma, V. Fornes, J. Martinez-Triguero, S. B. Pergher, *J. Catal.* **1999**, *186*, 57.
[15] S. van Donk, F. M. F. de Groot, O. Stephan, J. H. Bitter, K. P. de Jong, *Chem. Eur. J.* **2003**, *9*, 3106.
[16] M. Rozwadowski, J. Kornatowski, J. Wloch, K. Erdmann, R. Golembiewski, *Appl. Surf. Sci.* **2002**, *191*, 352.
[17] M. Ogura, S. Y. Shinomiya, J. Tateno, Y. Nara, M. Nomura, E. Kikuchi, M. Matsukata, *Appl. Catal. A* **2001**, *219*, 33.
[18] J. C. Groen, W. D. Zhu, S. Brouwer, S. J. Huynink, F. Kapteijn, J. A. Moulijn, J. Pérez-Ramírez, *J. Am. Chem. Soc.* **2007**, *129*, 355.
[19] A. H. Janssen, P. Van Der Voort, A. J. Koster, K. P. de Jong, *Chem. Commun.* **2002**, 1632.
[20] U. Ziese, K. P. de Jong, A. J. Koster, *Appl. Catal. A* **2004**, *260*, 71.
[21] H. Friedrich, P. E. de Jongh, A. J. Verkleij, K. P. de Jong, *Chem. Rev.* **2009**, *109*, 1613.
[22] K. S. W. Sing, D. H. Everett, R. A. W. Haul, L. Moscou, R. A. Pierotti, J. Rouquerol, T. Siemieniewska, *Pure Appl. Chem.* **1985**, *57*, 603.
[23] L. Karwacki, E. Stavitski, M. H. F. Kox, J. Kornatowski, B. M. Weckhuysen, *Angew. Chem.* **2007**, *119*, 7366; *Angew. Chem. Int. Ed.* **2007**, *46*, 7228.
[24] M. H. F. Kox, E. Stavitski, B. M. Weckhuysen, *Angew. Chem.* **2007**, *119*, 3726; *Angew. Chem. Int. Ed.* **2007**, *46*, 3652.
[25] L. Karwacki, M. H. F. Kox, D. A. M. de Winter, M. R. Drury, J. D. Meeldijk, E. Stavitski, W. Schmidt, M. Mertens, P. Cubillas, N. John, A. Chan, N. Kahn, S. R. Bare, M. Anderson, J. Kornatowski, B. M. Weckhuysen, *Nat. Mater.* **2009**, *8*, 959.
[26] J. R. Agger, N. Hanif, C. S. Cundy, A. P. Wade, S. Dennison, P. A. Rawlinson, M. W. Anderson, *J. Am. Chem. Soc.* **2003**, *125*, 830.
[27] E. G. Derouane, S. Detremmerie, Z. Gabelica, N. Blom, *Appl. Catal.* **1981**, *1*, 201.
[28] R. von Ballmoos, W. M. Meier, *Nature* **1981**, *289*, 782.
[29] N. Danilina, F. Krumeich, S. A. Castelanelli, J. A. van Bokhoven, *J. Phys. Chem. C* **2010**, *114*, 6640.
[30] M. H. F. Kox, A. Mijovilovich, J. Sattler, E. Stavitski, B. M. Weckhuysen, *ChemCatChem* **2010**, *2*, 564.
[31] E. Stavitski, M. R. Drury, D. A. M. de Winter, M. H. F. Kox, B. M. Weckhuysen, *Angew. Chem.* **2008**, *120*, 5719; *Angew. Chem. Int. Ed.* **2008**, *47*, 5637.

